Earth Planets Space, **61**, 689–701, 2009

Strong ground motions from an M_j 6.1 inland crustal earthquake in Hokkaido, Japan: the 2004 Rumoi earthquake

Takahiro Maeda[1] and Tsutomu Sasatani[2]

[1]*Institute of Seismology and Volcanology, Faculty of Science, Hokkaido University, N10W8 Kita-ku, Sapporo 060-0810, Japan*
[2]*Graduate school of engineering, Hokkaido University, N13W8 Kita-ku, Sapporo 060-8628, Japan*

(Received April 7, 2008; Revised September 30, 2008; Accepted October 30, 2008; Online published July 27, 2009)

An inland crustal earthquake (M_j 6.1) occurred on December 14, 2004 in the northern part of Hokkaido, Japan. A large ground acceleration of 1127 cm/s^2 and a large pseudo-velocity response of over 100 cm/s were recorded at the nearest strong-motion station, HKD020, about 10 km from the hypocenter. This large ground motion is considered to be attributable to the source effect and the site effect. The site effect is investigated using the traditional spectral ratio technique and the theoretical evaluation based on the subsurface structure model. The results imply that the site effect has an insignificant effect on the large ground motion at HKD020. The source effect is investigated by constructing the source model that explains the broad-band strong-motion records at four stations around the epicenter using the empirical Green's function method. The estimated source model satisfies the empirical relationship between the strong motion generation areas and the seismic moment for inland crustal earthquakes. The high-frequency level of the acceleration source spectrum is also consistent with the empirical relationship. These results suggest that this earthquake is a normal crustal event and that the large ground motion at HKD020 is mainly attributable to the source effect, short distance from the strong motion generation area and the forward directivity effect. Finally, the temporal change of the site response at HKD020 is examined using long duration records including the main shock and several aftershocks. The site response based on the S-wave horizontal-to-vertical spectral ratio method shows the nonlinearity for the main shock and an aftershock occurring about 20 s after the main shock. However, the site response shows linearity for other later aftershocks. This site response change is attributed to the difference in ground motion amplitude.

Key words: The 2004 Rumoi earthquake, strong ground motion, source model, empirical Green's function method, site response.

1. Introduction

A damaging crustal earthquake occurred in northern Hokkaido, Japan at 14:56 on December 14, 2004 (JST). The hypocenter is located in a southern Rumoi district; we call this earthquake the 2004 Rumoi earthquake in this paper. The moment magnitude (M_w) determined by the F-net Project of National Research Institute for Earth Science and Disaster Prevention (NIED) and Harvard University is 5.7. The focal depth and magnitude (M_j) determined by the Japan Meteorological Agency (JMA) is 8.6 km and 6.1, respectively. This is the first M_j 6 class crustal earthquake in Hokkaido since high density strong motion networks, such as K-NET and KiK-net operated by NIED, were deployed over Japan. A maximal seismic intensity of 5 lower on the JMA scale was observed at the northern side of the epicenter. A maximal ground acceleration of 1127 cm/s^2 was recorded at K-NET station HKD020 (Fig. 1) about 10 km from the hypocenter; the seismic intensity at HKD020 corresponds to 6 lower, but this is not an official intensity rating. During the earthquake, eight persons were injured and 165 houses were damaged (Sapporo District Meteorological Observatory, 2005). Following the main shock, many aftershocks occurred and some of them were recorded by the strong motion networks.

Hokkaido, the northern island of Japan, is situated in the plate convergence zone where the Amurian (Eurasia) plate is in collision with the Okhotsk (North American) plate, and the Pacific plate is subducting along the Kurile trench (Fig. 1). These plate motions accompany many interplate and intraslab earthquakes with magnitude 7 or more around Hokkaido, while large ($>M_j$ 6) inland crustal earthquakes have been rare. The 2004 Rumoi earthquake occurred in northwestern Hokkaido, where the seismicity of shallow crustal earthquake is relatively high and where recently several M_j 5 class earthquakes have occurred. The focal mechanism solutions (Fig. 1) indicate that the 2004 Rumoi earthquake occurred on a reverse fault with a W-NW to E-SE compression stress system. This compression axis is consistent with a regional stress field generated by a collision of the Amurian plate with the Okhotsk plate (e.g., Takahashi *et al.*, 1999).

In order to obtain a detailed aftershock distribution, an urgent seismic observation had been made immediately after the main shock in the source region (Maeda *et al.*, 2005; Ichiyanagi *et al.*, 2007). Nine temporary observation sites

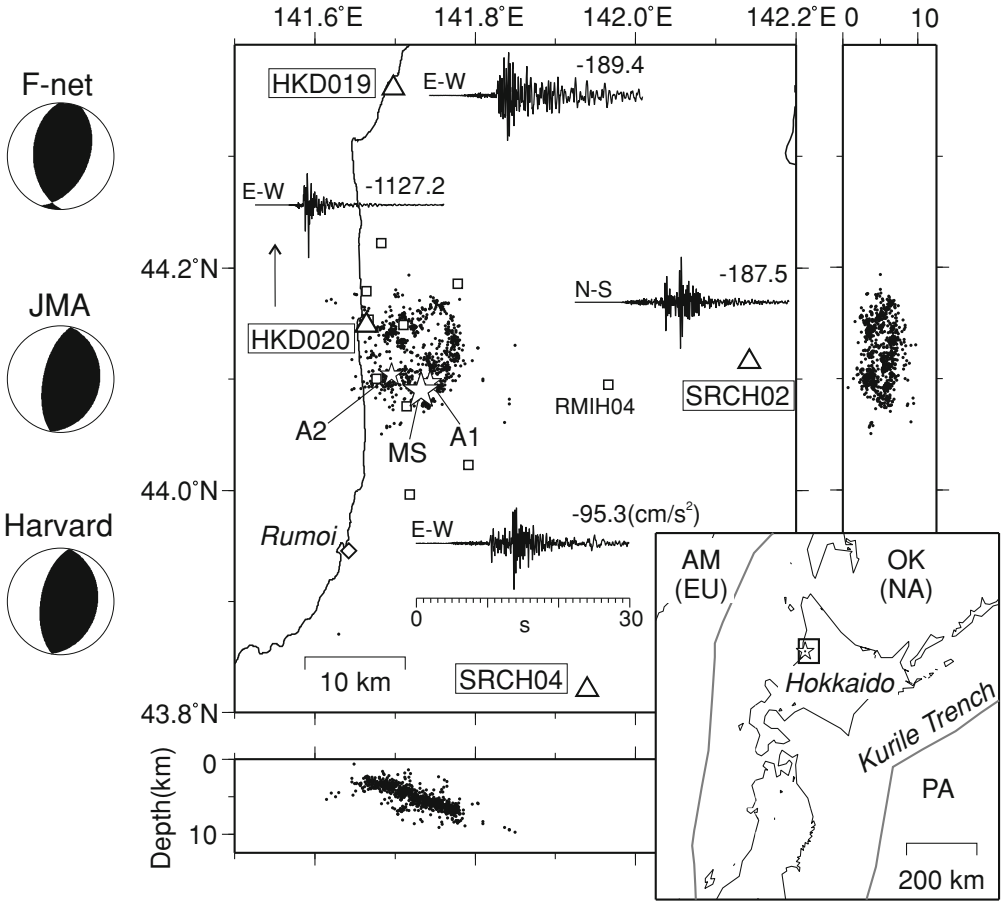

Fig. 1. Location map of the 2004 Rumoi earthquake. Open stars are epicenters of the main shock (MS) and aftershocks (A1, A2). Open squares indicate temporary and permanent stations used in determination of aftershocks (black dots) by Ichiyanagi *et al*. (2007). Observed accelerograms from the main shock at four strong-motion stations (triangles) are shown; the numbers attached to them are the peak amplitude. Focal mechanism solutions determined by F-net, JMA and Harvard University are shown; those from F-net and Harvard are CMT solutions and that from JMA is a first-motion solution. The study area is indicated by a square in the inset map. Abbreviations in the inset: EU, Eurasia; AM, Amurian; NA, North American; OK, Okhotsk; PA, Pacific plate.

were deployed from December 14, 2004 to middle of February, 2005 (Fig. 1). An east-dipping plane appears on E-W cross section of the well-determined aftershock distribution (Fig. 1). One nodal plane of the main-shock focal mechanism corresponds to this plane. GPS observation also estimates the east-dipping plane as a fault plane (Geographical Survey Institute, 2004).

Around the source region, two active faults (Hirotomi fault and Rikibiru fault) have been recognized. These active faults, however, show a west-dipping plane conjugate to the fault plane of the 2004 Rumoi earthquake. In addition, a surface fault relating to the 2004 Rumoi earthquake has not been confirmed. These facts indicate that the 2004 Rumoi earthquake occurred on an unrecognized blind faults. Tamura *et al*. (2005) suggested that the Hirotomi and Rikibiru faults are secondary fault generated by the major east-dipping blind fault.

The 2004 Rumoi earthquake provides us with a good opportunity to study strong ground motions from crustal earthquakes in Hokkaido. In particular, it is important to investigate the factors causing severe ground acceleration larger than 1 g from the moderate-size earthquake occurring on an unrecognized shallow fault. In this paper, we first examine characteristics of strong ground motions from the 2004 Rumoi earthquake. Next, we investigate two factors, site effect and source effect, in relation to the generation of large ground acceleration at HKD020. In addition, we examine a nonlinear site response at HKD020 during the main shock.

2. Strong Ground Motions

The 2004 Rumoi earthquake was recorded by the dense strong-motion networks and provides a large number of data enough to illustrate the regional scale characteristics of ground motions. Figure 2(left) shows a spatial distribution map of peak ground acceleration (PGA) values based on data from K-NET, KiK-net, and the seismic intensity network of the Hokkaido government. The PGA contour map shows an elliptical shape with the major axis in the N-S direction. In particular, a high PGA region extends to the northern side of the epicenter, suggesting unilateral rupture propagation from south to north.

Figure 2(right) shows an attenuation relationship of PGA values together with the empirical relationship for inland crustal earthquake (Si and Midorikawa, 1999). A fault distance is calculated using a fault plane model inferred from the well-determined aftershock distribution (Ichiyanagi *et al*., 2007; Fig. 6). The observed PGA values are compara-

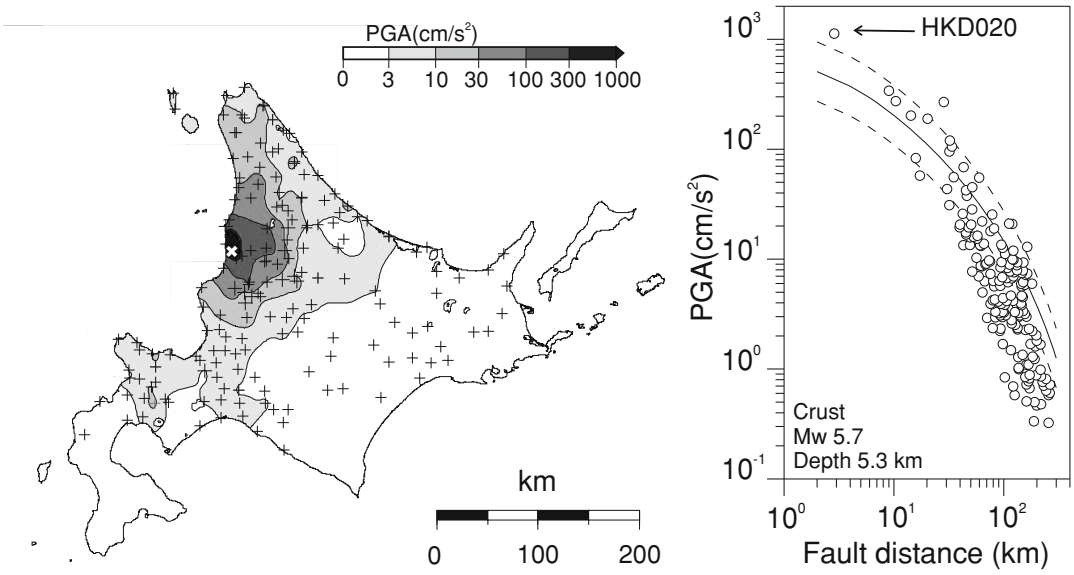

Fig. 2. Left: Spatial distribution of peak ground acceleration (PGA) from the 2004 Rumoi earthquake. PGA is a maximal value of a vector sum of three-component acceleration seismograms. Crosses are the strong-motion stations used in making the contour map. A white cross is the epicenter. Right: Attenuation relationship of PGA (largest value of two horizontal components). Fault distance is calculated using the fault plane shown in Fig. 6. The empirical relationship (solid curve) and standard deviations (dashed curves) proposed by Si and Midorikawa (1999) are also shown.

ble to the empirical one for distances less than 40 km, while the observed values are smaller than the empirical one for distances larger than 40 km. This feature indicates high attenuation property of the crust in the northern Hokkaido. In addition, we note that the PGA value at HKD020 exceeds one standard deviation of the empirical value.

Accelerograms at four stations surrounding the source region are shown in Fig. 1. Two *S*-wave pulses appear at SRCH02 and SRCH04; the second pulse has larger amplitude than the first one. These *S*-wave pulses are considered to be generated by the source process because the aftershock seismograms show a single *S*-wave pulse at these stations. Intervals of the *S*-wave pulses are about 3 s at the southern site (SRCH04), and 2 s at the eastern site (SRCH02). In this figure, however, two pulses are not recognized clearly at the northern sites (HKD019, HKD020). This azimuthal dependence of *S*-wave pulse interval suggests that the main shock consists of two subevents and that the second subevent occurs at the northern side of the first one. This hypothesis is consistent with the PGA spatial distribution shown in Fig. 2(left).

Figure 3(a) shows observed seismograms at HKD020 where peak acceleration of 1127 cm/s^2 and peak velocity of 75 cm/s were recorded. In this figure, two *S*-wave pulses are recognized on the velocity seismograms; the interval is less than 1 s. Figure 3(b) shows pseudo-velocity response spectra ($h = 5\%$) at HKD020 together with the empirical spectrum (Kanno *et al*., 2006). This empirical spectrum was originally provided as the horizontal acceleration response spectrum, therefore, we divided them by angular frequency and obtained the pseudo-velocity response. The E-W pseudo-velocity response spectrum is considerably larger than the empirical one and exceeds 100 cm/s for the period range of 0.32–0.6 s and around 1.5 s.

The 2004 Parkfield, California, earthquake (M_w 6.0) was recorded by an extensive set of strong-motion stations at a near-fault region. The strong motion records from this earthquake may be a good reference to understand the ground-motion level from M_w 6.0 event. The range of PGA is 0.13 g to 1.8 g (3 records exceed 1 g), and the largest peak ground velocity (PGV) is about 80 cm/s at three sites (Shakal *et al*., 2006). Shakal *et al*. (2006) pointed out that the largest accelerations occurred near the ends of the inferred rupture zone. They investigated the rupture directivity effect on the peak ground motions: the forward directivity effect for PGA was strong only close to the strike of the fault, near and beyond the ends of the faulting, and the effect for PGV was clearer than PGA. Liu *et al*. (2006) showed that very high PGAs corresponded to a large-amplitude shallow fault slip and that high PGVs could be explained in part by site effects.

The ground motion at HKD020 during the 2004 Rumoi earthquake is comparable to the largest ground motions of the 2004 Parkfield earthquake, though the two earthquakes have some differences; the Parkfield and Rumoi earthquakes are strike-slip and thrust events, surface and buried rupture events, and long and short fault length events, respectively. The factors causing large ground motions can be attributed to source and site effects, as shown in case of the Parkfield earthquake. In the following sections, we investigate the site and source effects on the observed strong ground motions at HKD020.

3. Site Effect

We investigate the site effect on the strong ground motions at HKD020 using the traditional spectral ratio technique (e.g., Borcherdt, 1970), which determines the site amplification at a specific site with respect to a nearby reference site. The site amplification is estimated by taking a ratio of amplitude spectrum at HKD020 to that at a reference site from the same source. We use bore-hole records at KiK-net RMIH04, about 25 km from HKD020 (Fig. 1)

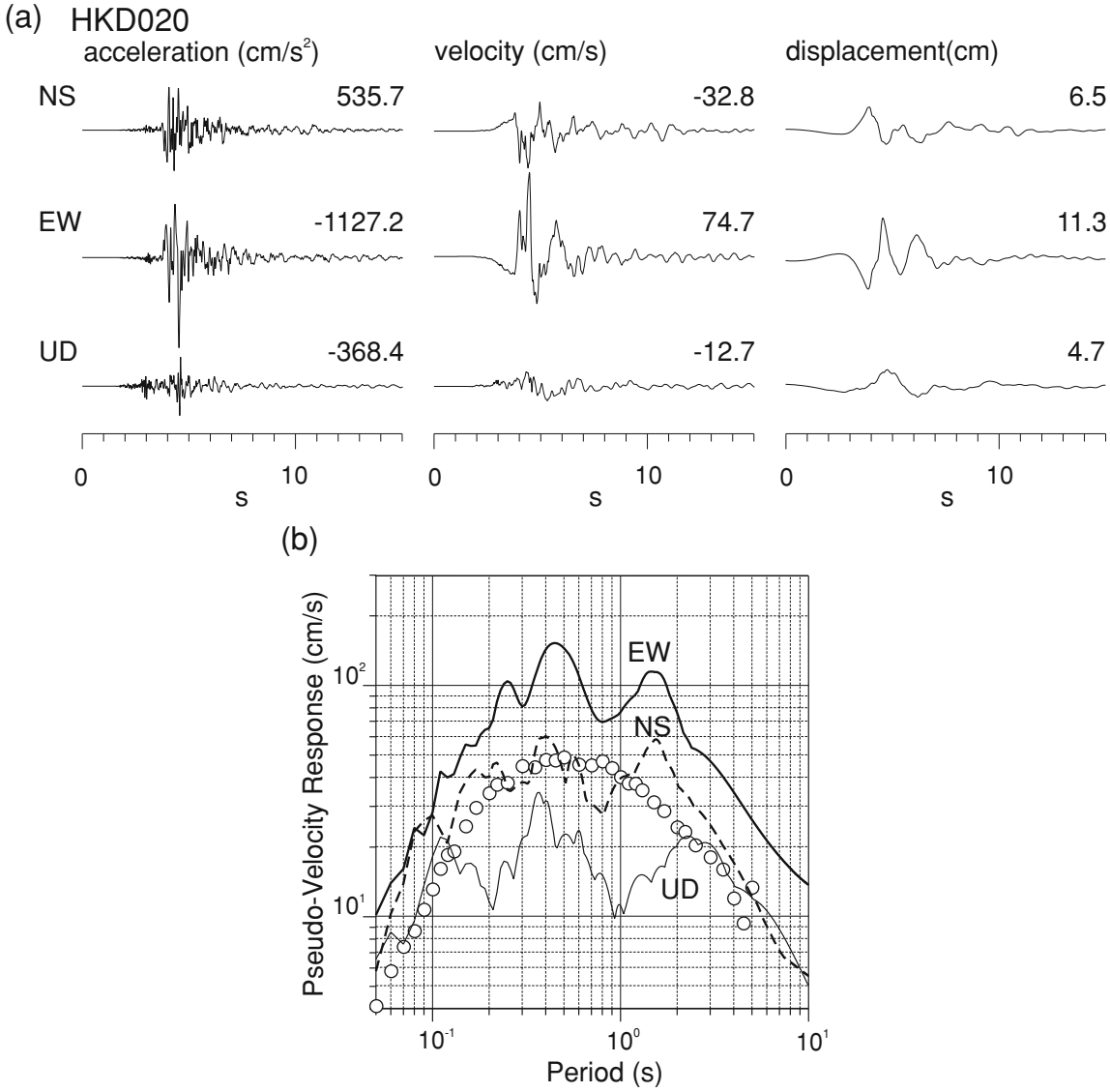

Fig. 3. (a) Observed waveforms at HKD020. (b) Pseudo-velocity response spectra at HKD020. Open circles are the response spectra based on the empirical relationship (Kanno *et al*., 2006).

as the reference; the sensor depth is 103 m. Fourier spectra are calculated from a 10.24-s time window, including the *S* wave, and then smoothed using the Parzen window (band width is 0.4 Hz). Two horizontal spectra are summed as vectors and corrected for the geometrical spreading effect. Figure 4(a) shows the spectral ratios of HKD020 to RMIH04 for the main shock and two aftershocks (Fig. 1). The aftershocks have a focal mechanism similar to the main shock. If the source and path effects were cancelled completely, all of the spectral ratios should show the similar shapes. However, the main-shock spectral ratio shows a peculiar feature in that spectral peaks appear approximately at 0.6 and 2 Hz, which are not found in the aftershock spectral ratios. This discrepancy in the spectral ratios indicates that the source effect as well as the path effect remains in the main-shock spectral ratio. The peak frequencies of the main-shock spectral ratio correspond to the period ranges of the large pseudo-velocity response (Fig. 3(b)). Therefore, the large pseudo-velocity response at HKD020 during the main shock is considered to be attributable to the source effect.

The site effect is also investigated theoretically using the subsurface structure model. The site amplification for the *SH* wave is simulated using the Propagator Matrix method (Aki and Richards, 1980). We analyze two structure models at HKD020. One is based on the logging data down to a 10-m depth provided by NIED. In this model, the engineering bedrock (*S*-wave velocity (V_S) ∼710 m/s and *N* value ∼99) appears at a 7-m depth. The other is the deeper structure model estimated by Maeda *et al*. (2008) using explores; the array measurement of microtremors (e.g., Okada, 2003), and the spectral analysis of surface waves. In this model, the V_S∼1400 m/s layer appears at a depth of 330 m. Figure 4(b) shows the theoretical site amplifications calculated from the above two structure models. The site response based on the logging data has a spectral peak at 20 Hz and represents the free surface amplification effect for frequencies less than 2 Hz, thus, the surficial layers contribute less to the large velocity response at HKD020. The site amplification based on the deeper structure model shows some spectral peaks

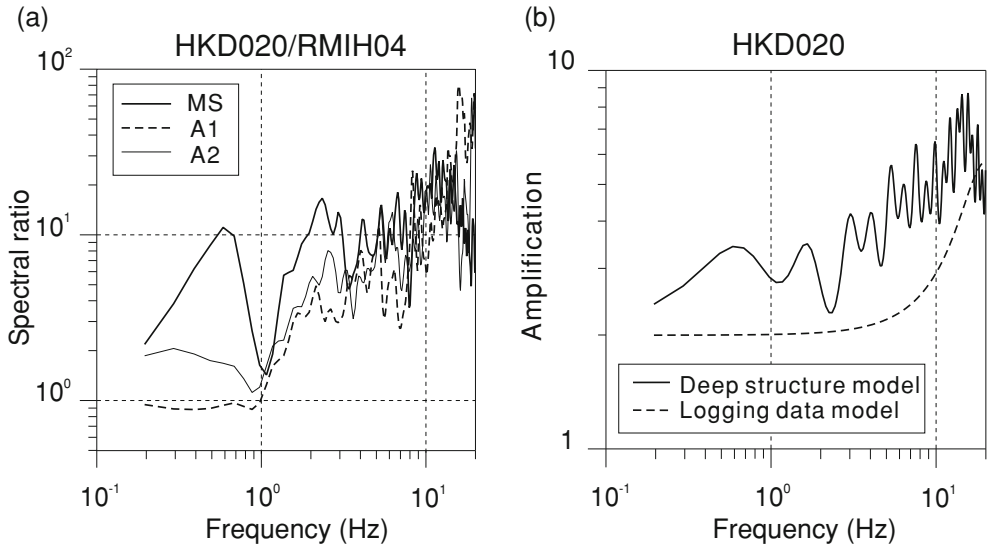

Fig. 4. (a) Spectral ratios between HKD020 and RMIH04 for the main shock (MS) and two aftershocks (A1 and A2); A1 (12/14/2004 16:06, M_w 3.5, this study), and A2 (12/14/2004 17:54, M_w 4.5, F-net); their locations are shown in Fig. 1. (b) Theoretical site amplification at HKD020. Solid and dashed lines are based on the deep structure model (Maeda *et al.*, 2008) and logging data model, respectively.

Table 1. Source parameters of the main shock and aftershock used in EGF modeling.

	Main shock	Aftershock
Date	2004/12/14, 14:56	2004/12/14, 16:06
Epicenter*	44.0897N, 141.7322E	44.0974N, 141.7438E
Depth (km)*	5.3	6.0
M_j	6.1	3.9
M_o (N m)	4.44×10^{17} (F-net)	2.8×10^{14} (this study)
S (km^2)	100†	0.49
$\Delta\sigma$ (MPa)‡		2.0

*This study, †aftershock area, ‡Brune (1970, 1971).

at lower frequencies. However, the amplification level is too small to explain the difference between the observed E-W pseudo-velocity response and empirical one (Fig. 3(b)). From these considerations, we believe that the site effect has an insignificant effect on the large velocity response at HKD020.

4. Source Effect

The source effect on the large ground motions at HKD020 is investigated by constructing a source model of the main shock. The source model, which reproduces the observed broad-band strong ground motions, is estimated using the empirical Green's function (EGF) method (Irikura, 1986; Irikura *et al.*, 1997; Kamae and Irikura, 1998). The EGF method synthesizes waveforms from a target earthquake (main shock) using waveforms from an elemental small earthquake (aftershock) occurring close to the target earthquake as Green's functions. This method is suitable for the source modeling of the 2004 Rumoi earthquake, because short-period seismic waves predominate in the strong-motion data.

The ground motion from a target event $U(t)$ is expressed as

$$U(t) = c\sum_{i=1}^{N}\sum_{j=1}^{N}\frac{r}{r_{ij}}F\left(t - t_{ij}\right) * u(t), \tag{1}$$

where

$$t_{ij} = \frac{r_{ij} - r_0}{V_S} + \frac{\xi_{ij}}{V_R} + \epsilon_{ij}, \tag{2}$$

$$F(t) = \delta(t) + \frac{1}{n'(1-e^{-1})}\sum_{k=1}^{(N-1)n'} e^{-\frac{K-1}{(N-1)n'}} \cdot\delta\left[t - \frac{(K-1)T}{(N-1)n'}\right], \tag{3}$$

and $u(t)$ is ground motion from an elemental event. r, r_{ij}, and r_0 are distances from a station to the elemental event, and (i, j) are the subfault and rupture start point, respectively. ξ_{ij} is a distance from the rupture start point to the (i, j) subfault. V_R and V_S are rupture velocity and S-wave velocity, respectively; $V_S = 3.0$ km/s is assumed. T is a rise time of the target event, n' is an arbitrary integer number to shift the artificial periodicity to a frequency higher than that of interest, and ϵ_{ij} is a random number to avoid an artificial periodicity resulting from subfault size and rupture velocity. $F(t)$ is a filter function to correct a difference between slip functions of the target and elemental events. c is a stress drop ratio of the target event to the elemental event. N is a scaling parameter expressed as $N = (M_{0t}/cM_{0s})^{1/3}$, where M_{0t} and M_{0s} are the seismic moments for the target and elemental events, respectively. This formulation can

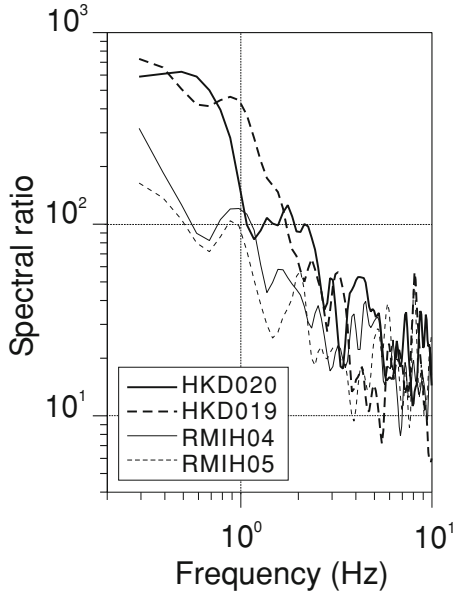

Fig. 5. Spectral ratios between the main shock and EGF aftershock at four stations.

be extended to cases of a multiple-shock event (Kamae and Irikura, 1998).

We assume that strong motions are generated from several strong motion generation areas (SMGAs) placed on the main-shock fault plane. Miyake *et al.* (2003) defined the area characterized by a large uniform slip velocity within the total rupture area as strong motion generation area and showed that the strong motion generation areas coincide with the asperity areas (areas of large slip). We assume two SMGAs on the fault plane of the 2004 Rumoi earthquake because two *S*-wave pulses are found in the observed waveforms (Figs. 1 and 3(a)). The geometry of the fault plane is inferred from the aftershock distribution obtained by the temporary observation (Ichiyanagi *et al*., 2007) and the main-shock focal mechanism solution; the fault plane has an area of 10 km×10 km with a strike and dip of 15° and 25° (Fig. 6).

An aftershock (M_j 3.9) occurring at 16:06, on 14 December 2007 is used as the elemental event, since this aftershock shows a simple *S*-wave waveform at the stations used in the modeling. Although the focal mechanism of the elemental aftershock after F-net is quite different from that of the main shock, we found that the elemental aftershock has the focal mechanism similar to the main shock, as shown in Appendix.

The hypocenters of the main shock and elemental aftershock have been determined using the permanent seismic network, since they occurred before the temporary observation. In order to determine the hypocenters of these earthquakes with a high degree of accuracy, we use two sets of aftershock hypocenters reported by Ichiyanagi *et al.* (2007); one is based on the temporary network and the other is based on the permanent network. We evaluate a systematic difference between the two sets of hypocenters and then apply it to the hypocenters of the main shock and elemental aftershock. As a result, the main shock is located near the southernmost tip of the aftershock area; the focal depth (5.3 km) is shallower than the JMA unified catalogue (8.6 km). The source parameters and relocated hypocenters for the main shock and elemental aftershock are shown in Table 1.

The positions and areas of the SMGA, stress drop ratios between the SMGA and elemental event, rise times of the SMGA, and average rupture velocity are estimated through the forward modeling of the acceleration, velocity, and displacement waveforms, and acceleration spectra at four stations shown below. The area of SMGA is evaluated in multiples of an elemental-event area; the elemental-event area is estimated by searching in the neighborhood of the value based on the Brune (1970, 1971) model and corner frequency of the source spectrum. Following Kamae *et al.* (1990), different effects of f_{max}, a high-frequency cutoff of the source spectra, between the main shock and elemental event are corrected using the function $1/(1 + (f/f_{max})^n)$. We roughly estimate these parameters using the observed spectra and then obtain appropriate values through the modeling; f_{max} for the main shock is 5.5 Hz and that for the elemental event is 10 Hz, and $n = 1.5$. We compare the observed and synthetic data at two K-NET (HKD019, HKD020) and two KiK-net (RMIH04, RMIH05) stations for the frequency band of 0.3–10 Hz; bore-hole records (at about 100 m depth) are used for the KiK-net stations.

Before beginning the EGF modeling, we show spectral ratios between the main shock and elemental aftershock at the four stations (Fig. 5). By taking a spectral ratio, path and site effects are cancelled, and thus source effect will remain. Spectral ratios are calculated in the same way as the traditional spectral ratio technique. The spectral ratios at northern sites (HKD019, HKD020) have higher corner frequencies and steeper spectral decays compared with those at eastern and southern sites (RMHI04, RMIH05). According to Miyake *et al.* (2001), this azimuthal dependence of spectral ratio represents the rupture directivity effect of the unilateral rupture propagation to the north.

After many trials, we obtain the source model and the parameters for SMGAs as shown in Fig. 6 and Table 2. The rupture velocity is estimated to be 2.7 km/s. The first SMGA is located around the hypocenter, and the second SMGA is located on a shallower part than the first one; the area of the second SMGA is four times larger than the first one. The azimuthal dependence of *S*-wave pulse interval constrains the second SMGA position relative to the first SMGA and the rupture velocity. The duration and amplitude of *S*-wave pulses constrain the size and stress drop of the SMGAs. The synthetic waveforms fit the observations well in both shape and amplitude (Fig. 7). The large-amplitude two velocity pulses observed at HKD020 are especially well replicated. The synthetic acceleration spectra also fit the observations well, as shown in Fig. 8. We recognize that HKD020 is located on a short distance (∼5 km) from the second (main) SMGA and in a forward direction of the rupture.

Characteristics of the obtained source model are examined by comparing the source parameters with those reported in the previous studies. Figure 9 shows relationships between the SMGA parameters and seismic moment M_0. In this figure, SMGA parameters (Miyake *et al*., 2003)

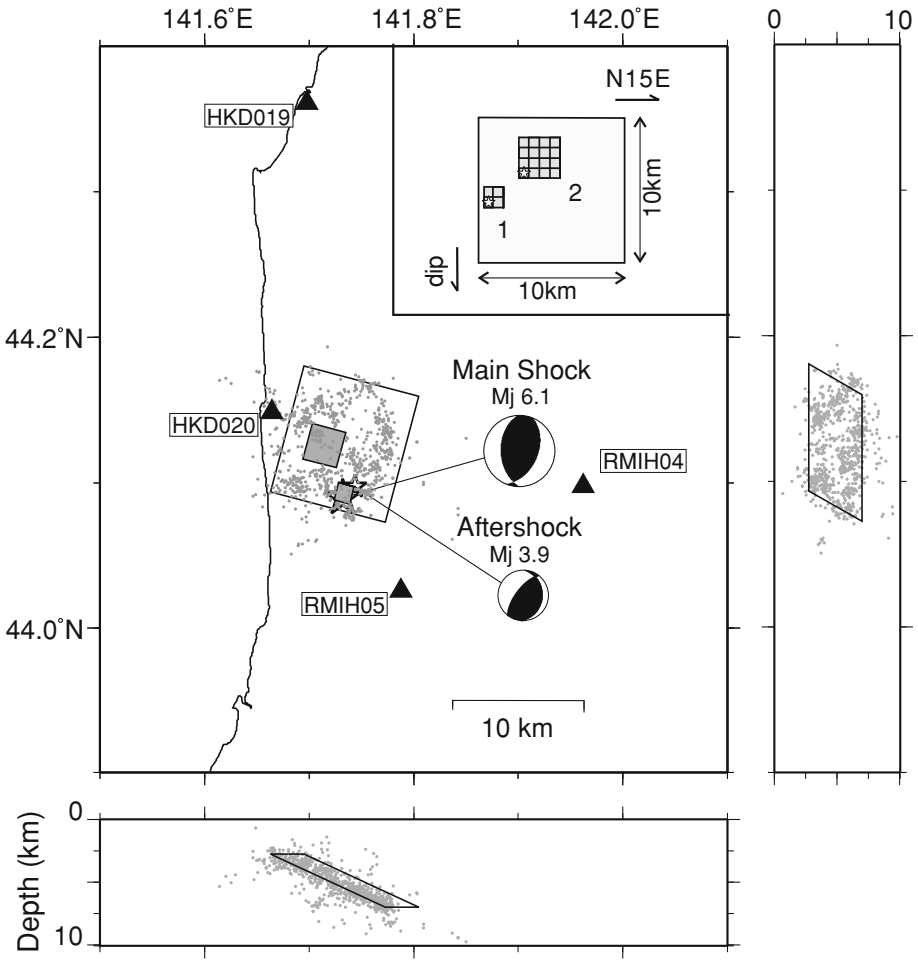

Fig. 6. Source model of the 2004 Rumoi earthquake based on the EGF method. Solid triangles are strong-motion stations used in the EGF modeling. Open and gray rectangles are the assumed fault plane and estimated SMGAs, respectively. Open stars are the epicenter of the main shock and elemental aftershock. Focal mechanisms of the main shock (after F-net) and the elemental aftershock (this study) are also shown. The inset shows the source model; stars represent start points of rupture.

Table 2. Parameters for the SMGAs.

SMGA	M_0 (N m)	Area (km^2)	$\Delta\sigma$ (MPa)	Rise time (s)	Slip (m)
1	3.14×10^{16}	1.96	27.9	0.4	0.66
2	1.16×10^{17}	7.84	12.9	0.4	0.61
Total	1.48×10^{17}	9.8			

and asperity parameters (Somerville *et al.*, 1999) from inland crustal earthquakes are also shown. The combined area of SMGA, area of largest SMGA and rise time for the 2004 Rumoi earthquake all have approximately the same values as expected from the empirical relationships (Somerville *et al.*, 1999). In addition, we examine the high-frequency level of acceleration source spectrum A. The A value based on the multiple asperity model is expressed as $A = 4\pi {V_S}^2 \sqrt{\Sigma (r_n \Delta\sigma_n)^2}$, where r_n and $\Delta\sigma_n$ are the equivalent radius and stress drop of the n-th SMGA, respectively (Dan *et al.*, 2002). Substituting the parameters in Table 2 and $V_S = 3.0$ km/s into this equation, we obtain $A = 3.40 \times 10^{18}$ N m/s^2; this value is approximately the same value ($A = 4.04 \times 10^{18}$ N m/s^2) as that derived from the empirical $A - M_0$ relationship for shallow inland and interplate earthquakes (Dan *et al.*, 2001). These facts suggest that the 2004 Rumoi earthquake has normal source characteristics. Therefore, we conclude that the large ground motion at HKD020 is caused by the short distance from the main SMGA and the forward directivity effect—that is, the source effect.

5. Nonlinear Site Effect

During the main shock, high acceleration ground motions of over 100 cm/s^2 were observed at several stations (see Fig. 2(right)), thus, nonlinear site effects are expected at these stations. The nonlinear site effect is usually detected using the site response spectrum; nonlinearity causes the peak period of site response to be long and/or the spectral level of site response to be low at shorter periods. The traditional spectral ratio technique that we have mentioned before has been widely applied to evaluate the site

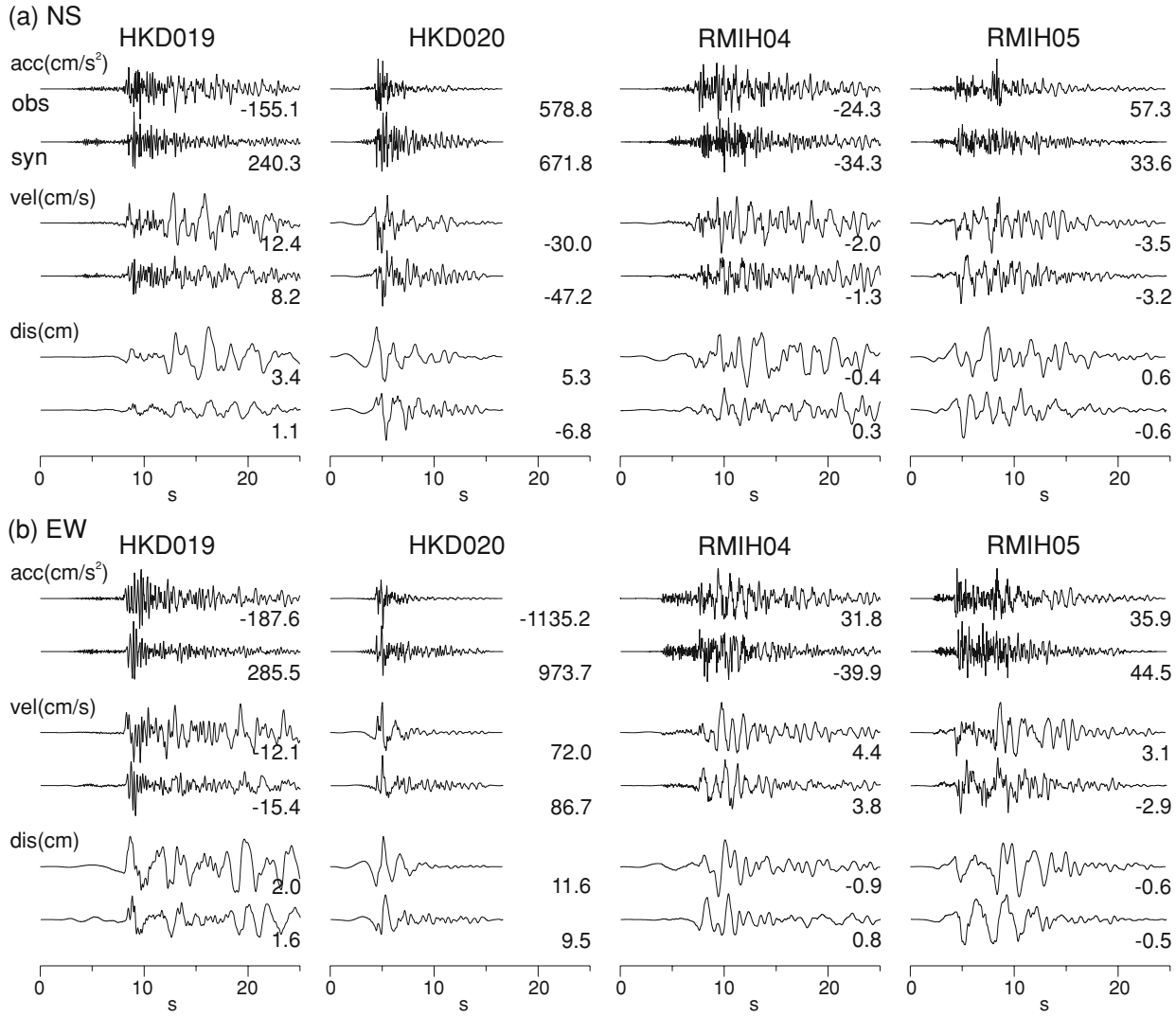

Fig. 7. Comparison of the observed waveforms (upper) with the synthetic waveforms (lower) calculated using the source model (Fig. 6); (a) N-S and (b) E-W components. Each column shows the acceleration (top), velocity (middle) and displacement (bottom) waveforms. The number on the lower right is the peak amplitude. All the waveforms are band-pass filtered for 0.3–10 Hz band and normalized by each peak amplitude.

response. In addition, the spectral ratio technique using a vertical array (surface vs. bore-hole) is also widely applied. These methods, however, need the reference site. The site response is also evaluated using a horizontal-to-vertical (H/V) spectral ratio of the S wave; we call this spectral ratio the S-H/V ratio hereafter. The S-H/V ratio is useful for detecting the nonlinear site effect, because it needs no reference site. In practice, Wen *et al.* (2006) proposed a technique for identifying the nonlinear site response using the S-H/V ratio of surface records at a single station. They demonstrated that the S-H/V ratio for strong motion data with the nonlinear response, which has been identified using vertical array data, shows the dominant period shift to longer period and the lower ratio level at short periods in comparison with the S-H/V ratio for weak motion data with the linear response. In our case, K-NET has only the surface instrument, and thus we evaluate the nonlinear site effect using the S-H/V ratio technique.

The S-H/V ratio is calculated from horizontal and vertical Fourier amplitude spectra. Horizontal and vertical spectra are calculated from a 10.24 s time window, starting 1 s before the S-wave arrival with a cosine-shaped taper of 10% each end of the window, and then smoothed using the Parzen window (band width is 0.4 Hz). A log-mean of two horizontal components is used as horizontal spectrum.

We examine the S-H/V ratios at the four stations used in the EGF modeling in the previous section; this modeling assumes a linear site response. The S-H/V ratios for the main shock and the EGF aftershock are compared with those for weak motions (Fig. 10). The peak accelerations of weak motions ($<$100 cm/s^2) are small enough to be considered a linear site response. The nonlinear characters of the response are clearly found in the S-H/V ratio for the main shock at HKD020, but these characters are not found at the other stations. The nonlinear characters, the peak-frequency shift, and amplitude reduction, appear at frequencies higher than 10 Hz and, therefore, the nonlinear site effect is considered to have little influence on the EGF modeling.

Strong motion data of the main shock at HKD020 have a long duration of 300 s, including the main shock and several aftershocks (Fig. 11). This record is useful to investigate a temporal change in the S-H/V ratios, which may

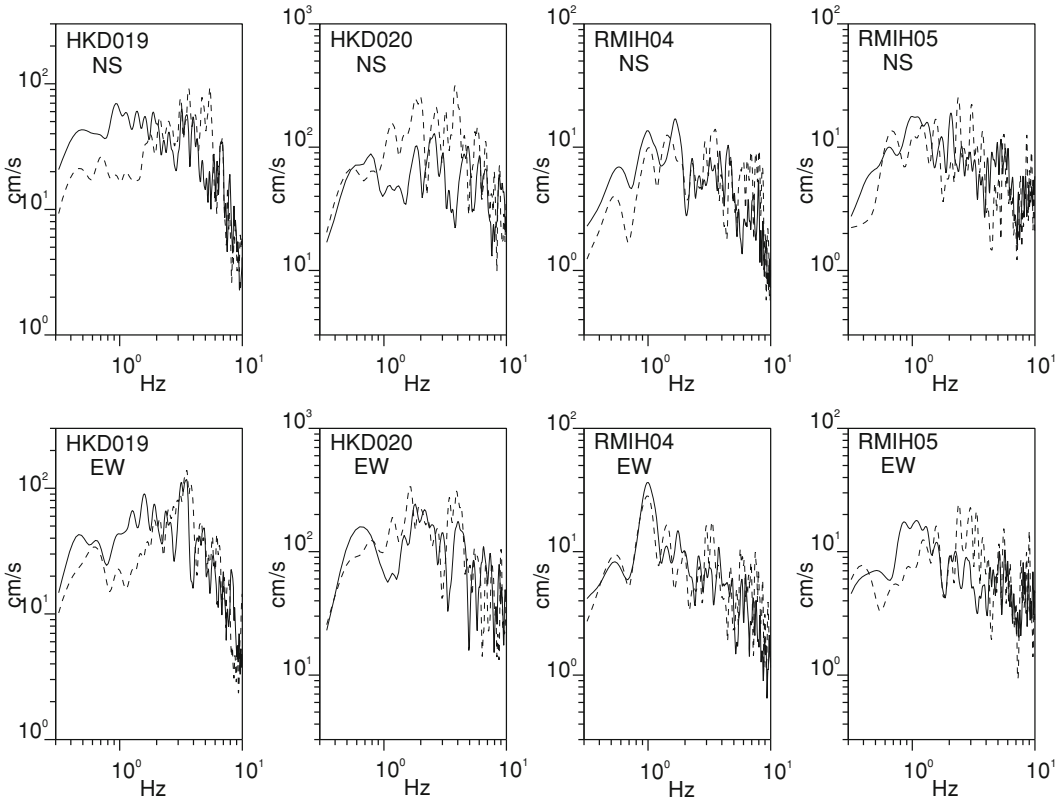

Fig. 8. Comparison between the observed and synthetic acceleration spectra for N-S (upper) and E-W (lower) components. Solid and dashed lines show the observed and synthetic spectra, respectively.

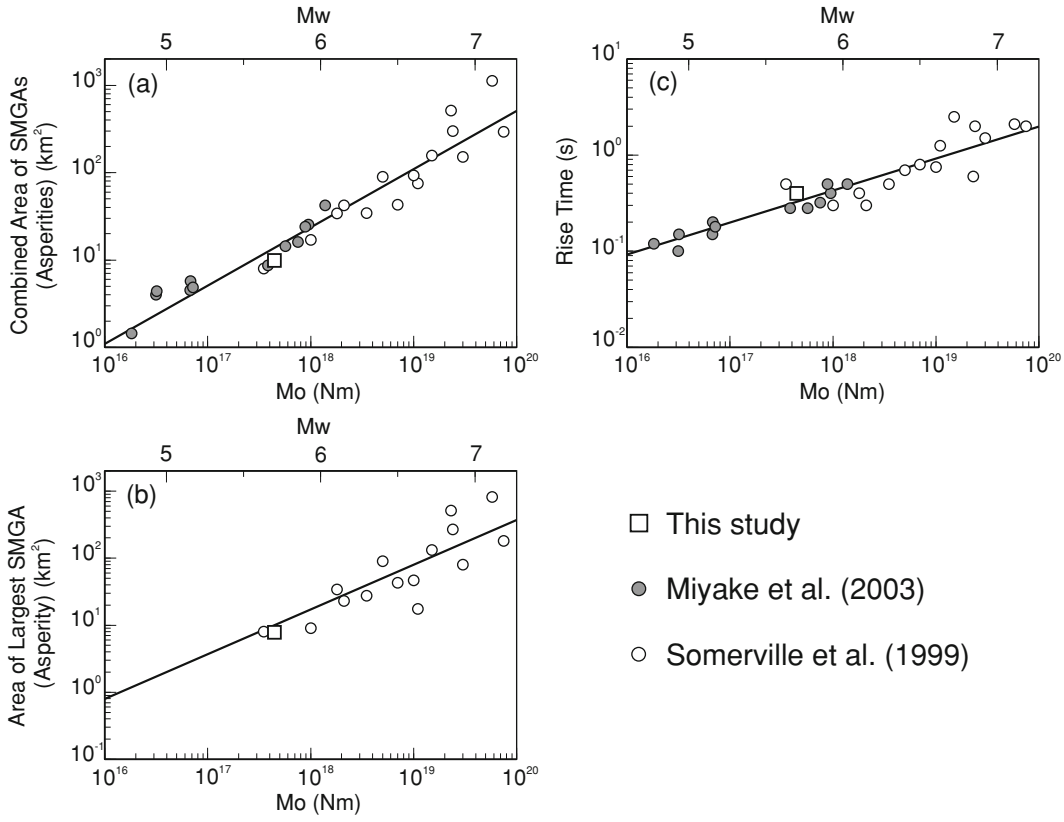

Fig. 9. Relationships between the source parameters and seismic moment; (a) combined area of SMGAs, (b) area of the largest SMGA, and (c) rise time. Parameters reported in Miyake *et al*. (2003) and Somerville *et al*. (1999) are also shown. Solid lines are the empirical relationships for asperity parameters (Somerville *et al*., 1999).

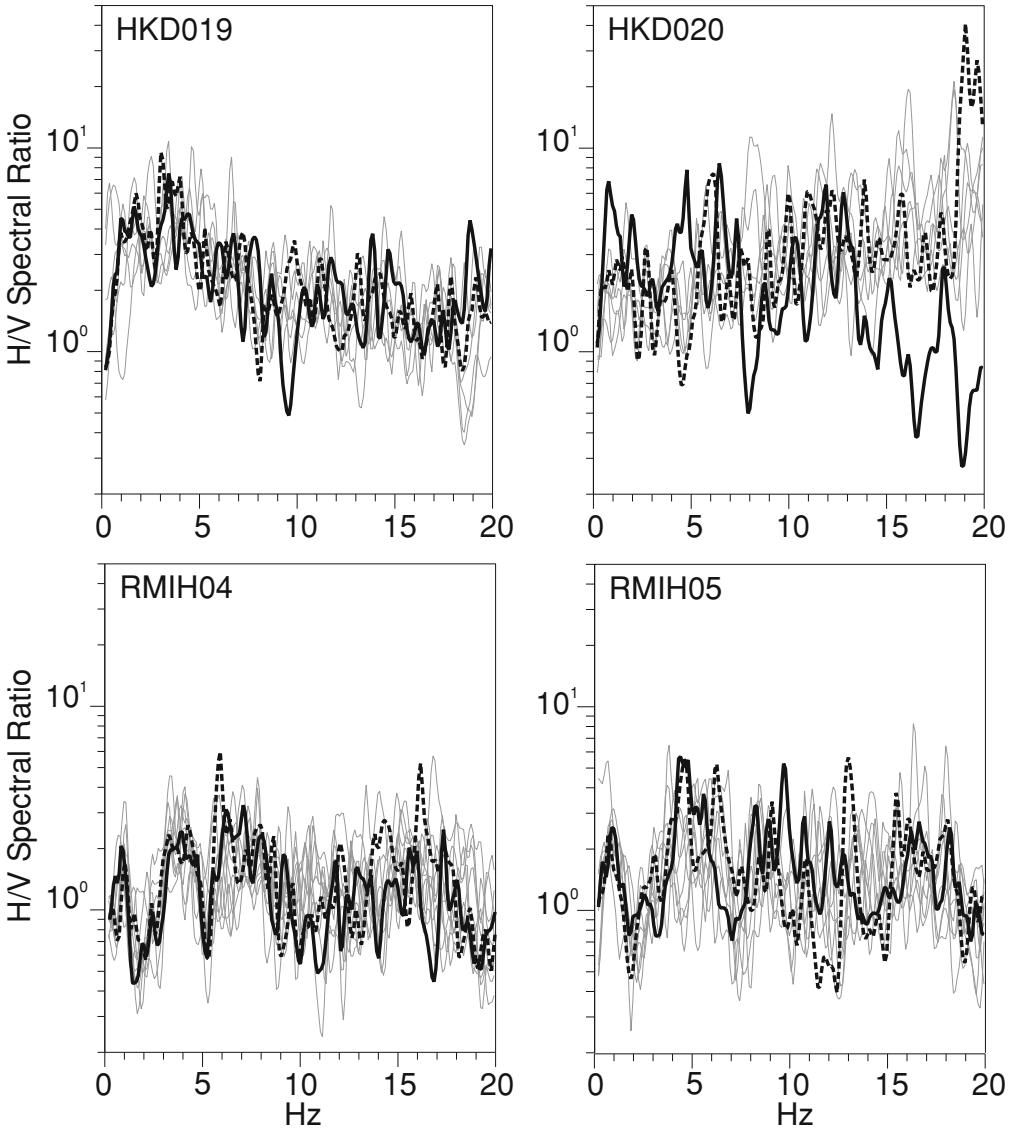

Fig. 10. *S*-wave horizontal-to-vertical spectral ratios at four stations. Bold and dashed lines show the spectral ratios for the main shock and the elemental aftershock used in the EGF modeling, respectively. Gray lines are the spectral ratios for weak motions ($<$100 cm/s^2).

represent a recovering process from the nonlinear site response to the linear response. We calculate S-H/V ratios for the main shock and the following five aftershocks and compare them with an averaged S-H/V ratio for weak motions (Fig. 11). Panel a (main shock) clearly shows the nonlinear response, as mentioned above. Panel b also shows the weak nonlinearity; the amplitude reduction at high frequencies. However, panels c–f (about 100 s after the main shock) show S-H/V ratios similar to those for weak motions, indicating the linear response. The difference between the S-H/V ratio character of panels a–b and c–f may represent the site response change with respect to the lapse of time—in other words, a recovering of site response from nonlinear to linear. However, alternatively, this may be due to the amplitude difference of ground motions; the peak amplitudes vary greatly between the panels a–b ($>$569 cm/s^2) and c–f ($<$82 cm/s^2). We consider that the difference of ground motion amplitude is a plausible interpretation of the site response change.

Aguirre and Irikura (1997) reported the nonlinear site response due to the liquefaction using spectral ratios between the surface and bore-hole *S*-wave records in Port Island, Kobe, during the 1995 Hyogo-ken Nanbu earthquake (M_w 6.9). They pointed out that the nonlinear character of the response appeared for at least 3 h after the main shock even for weak motions ($\sim$20 cm/s^2); that is, the permanence in the liquefaction state. Wen *et al*. (2006) applied the S-H/V ratio technique to the same data used in Aguirre and Irikura (1997) and obtained consistent results.

During the 2004 Rumoi earthquake, a septic tank about 10 m from the K-NET site was uplifted (Tamura *et al*., 2005). This uplift is probably due to the effect of the liquefaction of surficial soft soils. However, the effect of the liquefaction was not observed at the HKD020 site. The linear character for panels c–f (Fig. 11) also negate the liquefaction because the nonlinear character is expected even for the weak motions during the liquefaction state.

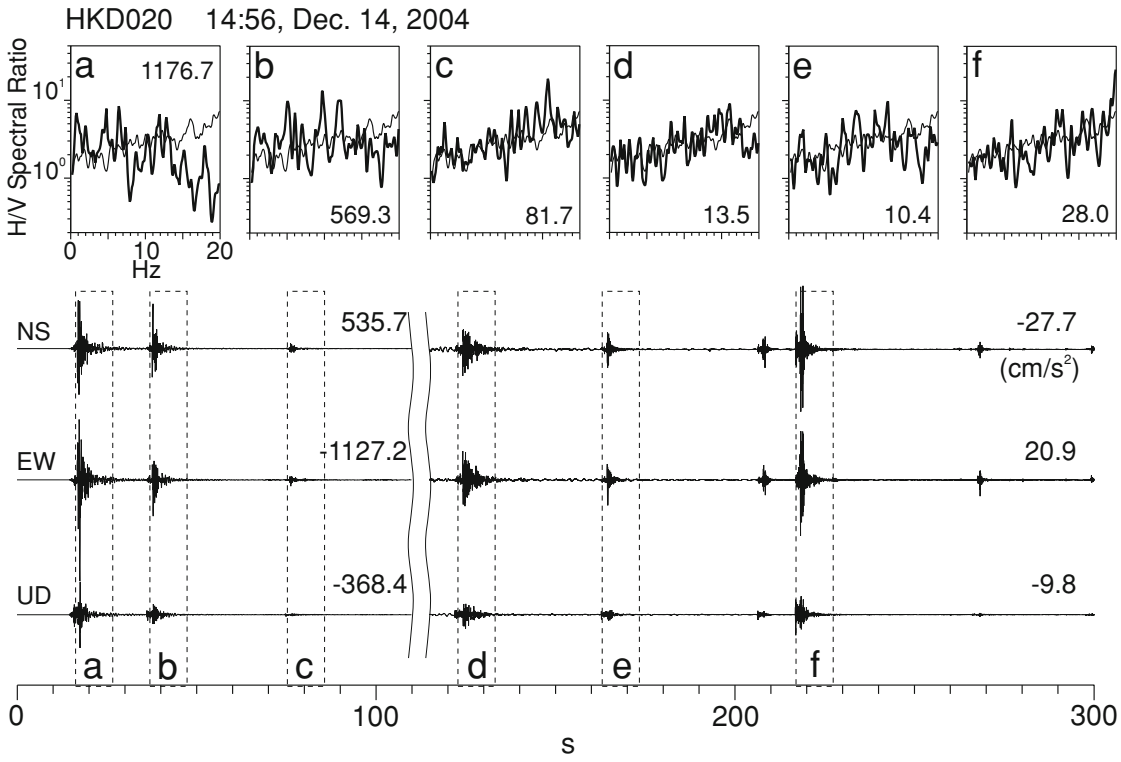

Fig. 11. Temporal change in the S-wave horizontal-to-vertical spectral ratios at HKD020 during the main shock (time window a) and following aftershocks (time windows from b to f). Three-component acceleration waveforms and the time windows are shown in the bottom. Bold and thin lines show the spectral ratio for each time window and the averaged one for weak motions (individual ratios are shown in Fig. 10 by gray lines). The number on each panel is the peak amplitude of a vector sum of three-component acceleration seismograms for the time window.

6. Conclusions

We investigated the factors causing severe ground motions at the K-NET HKD020 station during the 2004 Rumoi earthquake (M_j 6.1), which occurred on an unrecognized shallow fault. The site effect and source effect were considered to be a factor to cause such large ground motion. The site effect was investigated using the traditional spectral ratio technique and the theoretical evaluation based on the subsurface structure model. We concluded that the site effect has an insignificant effect on the large ground motion at HKD020. The source effect was investigated by constructing the source model using the empirical Green's function method. The obtained source model having two strong motion generation areas well explained the ground motions at HKD020 and at the surrounding three stations. The parameters for strong motion generation areas and the high-frequency level of acceleration source spectrum were consistent with the empirical relationships. Consequently, we concluded that the 2004 Rumoi earthquake is a normal crustal event and that the large ground acceleration and velocity response spectrum at HKD020 are mainly attributable to the source effect—short distance from the main strong motion generation area and forward directivity effect.

The nonlinear site effect was detected at HKD020 using the S-wave horizontal-to-vertical (S-H/V) spectral ratio. The S-H/V ratio for the early aftershock (about 20 s after the main shock) also showed a nonlinear character, while that for aftershock, about 100 s after the main shock, showed a linear character. This site response change was attributed to a difference of ground motion amplitude. These facts negate the occurrence of liquefaction at HKD020.

Acknowledgments. We thank K-NET, KiK-net, and F-net operated by the National Research Institute for Earth Science and Disaster Prevention for providing strong-motion data and moment tensor solutions; the Hokkaido government for providing strong-motion data; the Japan Meteorological Agency for providing hypocentral information and focal mechanisms; Harvard University for providing CMT solution. We are grateful to Masayoshi Ichiyanagi for his helpful support in the use of the hypocenter data, and Yasunori Nishida for improvement of this manuscript. This manuscript was greatly improved by constructive comments by Kenichi Kato and Yasumaro Kakehi. Some of the figures in this paper were made using GMT (Wessel and Smith, 1995).

Appendix A.

As mentioned in the text, the F-net focal mechanism of the elemental aftershock used in the EGF modeling is quite different from that of the main shock. The variance reduction of the CMT solution for the aftershock is low (54.91/100), suggesting lower reliability of the focal mechanism and seismic moment (M_0). In this appendix, we re-estimate the seismic moment (M_0) and focal mechanism of the elemental aftershock.

The optimal fault parameters (strike, dip, rake) and seismic moment are determined using the grid search by minimizing a residual between the observed and synthetic waveforms for the frequency band of 0.1–1.0 Hz. We use the observed velocity waveforms at three stations (HKD020, RMIH04, RMIH05) surrounding the epicenter. The synthetic waveforms are simulated using the discrete

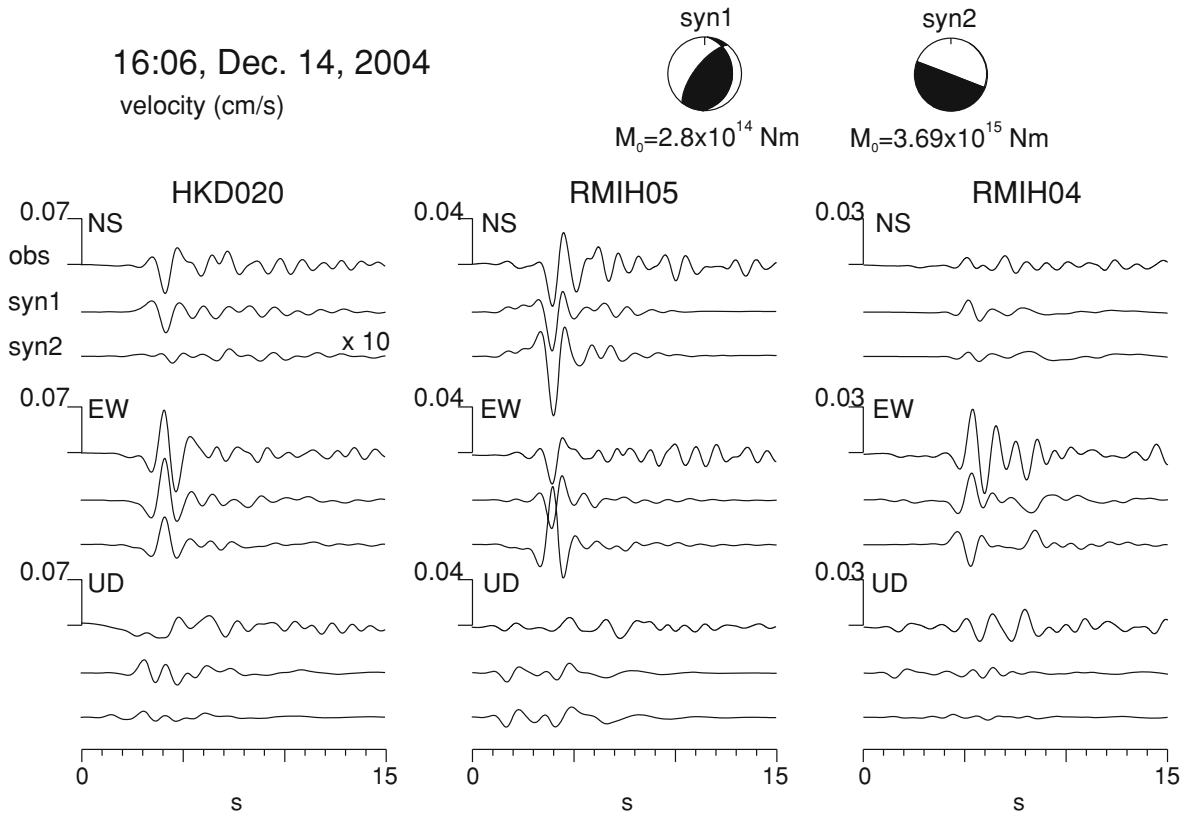

Fig. A.1. Comparison of the observed velocity waveforms from the elemental aftershock (16:06, Dec. 14, 2004) with the synthetic ones calculated using two kinds of focal mechanism and seismic moment (syn1 and syn2) at three stations. The syn1 model is estimated in this study, and the syn2 model is the CMT solution determined by F-net. Each column shows the NS, EW, and UD components of the waveform. All waveforms are band-pass filtered for 0.1–1.0 Hz band. The syn1 model gives close agreement with the observation. Note that the waveforms for the syn2 model are depicted on a scale of 1/10 compared with the others.

Table A.1. Subsurface structure model.

V_P km/s^2	V_S km/s^2	Density g/cm^3	Depth km	Q_P	Q_S
HKD020 (K-NET, LD 10 m*)					
0.380	0.160	1.6	0.000	150	70
0.740	0.300	1.6	0.001	150	70
1.380	0.500	2.0	0.003	200	100
2.000	0.710	2.0	0.007	200	100
3.500	1.850	2.2	1.000	300	150
4.493	2.567	2.3	2.000	600	300
4.955	2.831	2.7	4.000	600	300
RMIH04 (KiK-net, LD 103 m)					
2.060	0.310	2.0	0.000	200	100
2.060	0.510	2.0	0.002	200	100
2.060	0.690	2.0	0.018	200	100
2.060	0.830	2.0	0.036	200	100
2.510	0.950	2.1	0.084	300	150
3.500	1.850	2.2	1.000	300	150
4.493	2.567	2.3	2.000	600	300
4.955	2.831	2.7	4.000	600	300

Table A.1. (coninued).

V_P km/s^2	V_S km/s^2	Density g/cm^3	Depth km	Q_P	Q_S
RMIH05 (KiK-net, LD 108 m)					
0.360	0.150	1.6	0.000	150	70
1.740	0.150	2.0	0.002	200	100
1.740	0.390	2.0	0.016	200	100
1.740	0.580	2.0	0.024	200	100
2.380	0.920	2.1	0.034	300	150
2.760	1.180	2.1	0.086	300	150
3.500	1.850	2.2	1.000	300	150
4.493	2.567	2.3	2.000	600	300
4.955	2.831	2.7	4.000	600	300

*LD, depth of logging data.

wavenumber method (Bouchon, 1981; Takeo, 1985) assuming a 1-D stratified velocity structure for each station and a simple source time function (an isosceles triangle with a pulse width of 0.3 s). Each 1-D structure model (Table A.1) is based on logging data (∼100 m depth for KiK-net and ∼10 m depth for K-NET) and regional structure model (Moriya, 1986; Ichiyanagi *et al.*, 2007); Q values are based on the experience.

Figure A.1 shows the obtained focal mechanism solution and comparison of the observed and synthetic waveforms. This focal mechanism shows a thrust event, (strike, dip, rake) = (4°, 26°, 59°), and fully explains S-wave polarities at the stations. Synthetic waveforms assuming the CMT solution determined by F-net (syn2 in Fig. A.1) are quite different from the observed ones in amplitude and polarity. The seismic moment, $M_0 = 2.8 \times 10^{14}$ N m, is ap-

proximately thirteenth of the M_0 determined by F-net. The seismic moments and stress drops of the SMGA (Table 2) were calculated using this re-estimated M_0 value.

References

Aki, K. and P. G. Richards, *Quantitative Seismology*, **1**, 557 pp., W. H. Freeman and Company, 1980.

Aguirre, J. and K. Irikura, Nonlinearity, liquefaction, and velocity variation of soft soil layers in Port Island, Kobe, during the Hyogo-ken Nanbu earthquake, *Bull. Seismol. Soc. Am.*, **87**, 1244–1258, 1997.

Borcherdt, R. D., Effects of local geology on ground motion near San Francisco Bay, *Bull. Seismol. Soc. Am.*, **60**, 29–61, 1970.

Bouchon, M., A simple method to calculate Green's functions for elastic layered media, *Bull. Seismol. Soc. Am.*, **71**, 959–971, 1981.

Brune, N., Tectonic stress and the spectra of seismic shear waves from earthquakes, *J. Geophys. Res.*, **75**, 4997–5009, 1970.

Brune, N., Correction, *J. Geophys. Res.*, **76**, 5002, 1971.

Dan, K., M. Watanabe, T. Sato, and T. Ishii, Short-period source spectra inferred from variable-slip rupture models and modeling of earthquake faults for strong motion prediction by semi-empirical method, *J. Struct. Contr. Eng. AIJ*, **545**, 51–62, 2001 (in Japanese with English abstract).

Dan, K., T. Sato, and K. Irikura, Characterizing source model for strong motion prediction based on asperity model, *Proc. 11th Jpn. Earthq. Eng. Symp.*, 555–560, 2002 (in Japanese with English abstract).

Geographical Survey Institute, http://www.gsi.go.jp/WNEW/PRESS-RELEASE/2004/1215.htm, 2004.

Ichiyanagi, M., T. Maeda, T. Yamaguchi, H. Takahashi, M. Kasahara, T. Sasatani, and A. Yamamoto, Aftershock distribution of the December 14, 2004 Rumoi-nanbu earthquake (M 6.1) in the northern part of Hokkaido, Japan, *Zisin 2*, **59**, 209–221, 2007 (in Japanese with English abstract).

Irikura, K., Prediction of strong acceleration motions using empirical Green's function, *Proc. 7th Jpn. Earthq. Eng. Symp.*, 151–156, 1986.

Irikura, K., T. Kagawa, and H. Sekiguchi, Revision of the empirical Green's function method by Irikura (1986), *Proc. Seismol. Soc. Jpn. 2*, **B25**, 1997 (in Japanese).

Kamae, K. and K. Irikura, Source model of the 1995 Hyogo-ken Nanbu earthquake and simulation of near-source ground motion, *Bull. Seismol. Soc. Am.*, **88**, 400–412, 1998.

Kamae, K., K. Irikura, and Y. Fukuchi, Prediction of strong ground motion for M 7 earthquake using regional scaling relations of source parameters, *J. Struct. Constr. Eng. AIJ*, **416**, 57–70, 1990 (in Japanese with English abstract).

Kanno, T., A. Narita, N. Morikawa, H. Fujiwara, and Y. Fukushima, A new attenuation relation for strong ground motion in Japan based on recorded data, *Bull. Seismol. Soc. Am.*, **96**, 879–897, 2006.

Liu, P., S. Custódio, and R. J. Archuleta, Kinematic inversion of the 2004 M 6.0 Parkfield earthquake including an approximation to site effects, *Bull. Seismol. Soc. Am.*, **96**, S143–S158, doi:10.1785/120050826, 2006.

Maeda, T., T. Sasatani, M. Ichiyanagi, T. Yamaguchi, H. Takahashi, and M. Kasahara, The earthquake of December 14, 2004 (M 6.1) at southern Rumoi district, the northern part of Hokkaido, *Geophys. Bull. Hokkaido Univ.*, **68**, 243–253, 2005 (in Japanese with English abstract).

Maeda, T., N. Takai, and T. Sasatani, Site effect on large ground motion at HKD020 during the 2004 Rumoi earthquake, *Proc. Jpn. Assoc. Earthq. Eng.*, 2008 (in Japanese).

Miyake, H., T. Iwata, and K. Irikura, Estimation of rupture propagation direction and strong motion generation area from azimuth and distance dependence of source amplitude spectra, *Geophys. Res. Lett.*, **28**, 2727–2730, 2001.

Miyake, H., T. Iwata, and K. Irikura, Source characterization for broadband ground-motion simulation: kinematic heterogeneous source model and strong motion generation area, *Bull. Seismol. Soc. Am.*, **93**, 2531–2545, 2003.

Moriya, T., Seismo-tectonics of Hokkaido based on shallow seismicity and focal mechanism studies, in *Geology and Tectonics of Hokkaido*, *Monogr. Assoc. Geol. Collab. Jpn.*, **31**, 475–485, 1986 (in Japanese with English abstract).

Okada, H., *The Microtremor Survey Method (Geophysical monographs series no. 12)*, 135 pp., Society of Exploration Geophysicists, 2003.

Sapporo District Meteorological Observatory, *Reports of the southern Rumoi district earthquake on December 14th, 2004*, 2005 (in Japanese).

Shakal, A., H. Haddadi, V. Graizer, K. Lin, and M. Huang, Some key features of the strong-motion data from the M 6.0 Parkfield, California, earthquake of 28 September 2004, *Bull. Seismol. Soc. Am.*, **96**, S90–S118, doi:10.1785/0120050817, 2006.

Si, H. and S. Midorikawa, New attenuation relationships for peak ground acceleration and velocity considering effects of fault type and site condition, *J. Struct. Constr. Eng. AIJ*, **523**, 63–70, 1999 (in Japanese with English abstract).

Somerville, P., K. Irikura, R. Graves, S. Sawada, D. Wald, N. Abrahamson, Y. Iwasaki, T. Kagawa, N. Smith, and A. Kowada, Characterizing crustal earthquake slip models for the prediction of strong ground motion, *Seismol. Res. Lett.*, **70**, 59–80, 1999.

Takahashi, H., M. Kasahara, F. Kimata, S. Miura, K. Heki, T. Seno, T. Kato, N. Vasilenko, A. Ivashchenko, V. Bahtiarov, V. Levin, E. Gordeev, F. Korchagin, and M. Gerasimenko, Velocity field of around the sea of Okhotsk and sea of Japan regions determined from a new continuous GPS network data, *Geophys. Res. Lett.*, **26**, 2533–2536, 1999.

Takeo, M., Near-field synthetic seismograms taking into account the effects of anelasticity—the effects of anelastic attenuation on seismograms caused by a sedimentary layer—, *Meteorol. Geophys.*, **36**, 235–257, 1985 (in Japanese with English abstract).

Tamura, M., G. Kawakami, T. Suzuki, N. Okazaki, and T. Oka, Preliminary observations on the 2004 Rumoi-shichou-nanbu earthquake—Geological damages, ground motion and the influence on hot spring well—, *Report of the geological survey of Hokkaido*, **76**, 113–128, 2005 (in Japanese).

Wen, K. L., T. M. Chang, C. M. Lin, and H. J. Chiang, Identification of nonlinear site response using the H/V spectral ratio method, *Terr. Atmos. Ocean. Sci.*, **17**, 533–546, 2006.

Wessel, P. and W. H. Smith, New version of the Generic Mapping Tools released, *EOS Trans. AGU*, **329**, 1995.

T. Maeda (e-mail: tmaeda@mail.sci.hokudai.ac.jp) and T. Sasatani